Biomaterials Science

Antioxidant Properties of ALD Grown Nanoceria Films with Tunable Valency

Journal:	*Biomaterials Science*
Manuscript ID	BM-ART-03-2019-000397.R1
Article Type:	Paper
Date Submitted by the Author:	01-May-2019

Complete List of Authors:	Gupta, Ankur; University of Central Florida Selvan, Tamil; University of central florida, Advanced Materials Processing and Analysis Center (AMPAC), NanoScience Technology Center (NSTC), Materials Science Engineering Neal, Craig; University of Central Florida, Advanced Materials Processing and Analysis Center, Materials Science and Engineering Koul, Supriya; University of Central Florida Singh, Sushant; University of Central Florida, Material Science and Engineering Kushima, Akihiro; University of Central Florida Seal, Sudipta; University of Central Florida, NanoScience Technology Center; University of Central Florida, Materials Science and Engineering

Journal Name

ARTICLE

Antioxidant Properties of ALD Grown Nanoceria Films with Tunable Valency

Received 00th January 20xx,
Accepted 00th January 20xx

DOI: 10.1039/x0xx00000x

www.rsc.org/

Ankur Gupta,[a,b,e] Tamil S. Sakthivel,[b] Craig J. Neal,[a,b] Supriya Koul,[a,b] Sushant Singh,[b] Akihiro Kushima,[a,b] and Sudipta Seal [a,b,c,d,e]

Herein, we provide the first account of a method to control cerium oxide's mixed valence states (as Ce^{3+} to Ce^{4+} ratio) in ultra-thin films formed via atomic layer deposition (ALD). It is determined that modulation of Ce^{3+}/Ce^{4+} ratio occurs with respect to film thickness and is analogous to the change in surface chemistry observed for cerium oxide nanoparticles with varying particle diameter. The influence of film thickness on enzyme-mimetic radical scavenging is also characterized. Higher film thicknesses show 9-fold increase in catalytic activity. In vitro biocompatibility (apoptosis <4%) and electrochemical biosensing (lowest concentration: 18 ppt) studies were performed to demonstrate the potential of ALD-grown nanoceria films for biomedical applications.

Introduction

Cerium oxide has been utilized in many technological applications for oxygen sensors [1,2], solid oxide fuel cells [3], catalytic converters [4,5], corrosion-resistant coatings [6,7], slurries in chemical mechanical planarization (CMP) [8,9], high *k*-dielectric material [10], etc. Magnetron-sputtered CeO_2 thin films on SiO_2 substrates have also been explored as optical waveguides [11]. Further, CeO_2 thin films have seen use as a buffer layer between substrate (Si or sapphire) and $YBa_2Cu_3O_7$ active layer in High-T_c superconductors [12,13]. High dielectric constant, dielectric strength, and moderate band gap also recommend CeO_2 as a potential high *k*-dielectric material for CMOS devices. Other factors such as lattice constant (Si 5.431 Å and CeO_2 5.411 Å; mismatch 0.36%) and thermodynamic stability also suggest it as a strong, potential candidate in this application [14-16].

Cerium atoms exist in dual oxidation state (Ce^{3+} and Ce^{4+}) in a metal oxide and, due to low reduction potential, cerium oxide exhibits redox-cycling behavior [17]. Upon conversion of a Ce^{4+} ion to Ce^{3+} ion, two oxygen vacancies are generated in the cerium oxide lattice; therefore, it also acts as an oxygen buffer [18]. Due to the redox cycling and low redox potential property, cerium oxide nanoparticles (CNPs) have shown efficacy as an antioxidant material for scavenging reactive oxygen species (ROS) and reactive nitrogen species (RNS). CNPs having a higher Ce^{3+}/Ce^{4+} ratio scavenge superoxide and hydroxyl radicals (OH*); whereas, lower Ce^{3+}/Ce^{4+} ratio CNPs scavenge hydrogen peroxide (H_2O_2) and nitroxy radicals (NO*) [19]. Furthermore, CNPs also regenerate surface redox state composition over time; therefore, antioxidant properties are long-lived and catalytic in nature [20]. Lee *et al* [20] have shown that oleic acid coated CNPs of 3.8 nm have 9-times higher reactivity than Trolex (commercial antioxidant). Oleic acid coated 3.8 nm CNPs can also regenerate their surface over 18-times in a period of 6 months. Cerium oxide has seen use in the healthcare field in varied applications including electrochemical biosensors [21,22], radiation protection [23], cancer therapeutic agent [24,25], radical scavenging [19] etc. CNPs were also found effective in ameliorating the deleterious effects of ischemic stroke [26] and free radical-mediated auto-immune/degenerative diseases in the brain [27]. Cerium oxide coatings on bio-implant surfaces also facilitate bone cell proliferation, in research literature [28].

Metallic orthopedic implants are commonly used in total hip and knee replacements, dental restoration and as a replacement for load-bearing bones, such as a femur, in the case of traumatic accidents. These metallic implants possess a thin layer of oxide on their surface, which help in tissue growth and proliferation due to their biocompatible nature. However, due to the highly corrosive environment within the human body and relative motion of a weight-bearing/support implant in association with the bone, wear debris is generated at the implant-bone interface. The interactions between wear debris and tissues results in inflammation and the generation of ROS from the immune system. This relationship has been observed

[a] Department of Materials Science and Engineering, University of Central Florida, 12760 Pegasus Blvd., P.O. Box 162450, Orlando, Florida 32816, United States
[b] Advanced Materials Processing and Analysis Center, University of Central Florida, 4000 Central Florida Blvd., P.O. Box 162455, Orlando, Florida 32816, United States
[c] Nanoscience Technology Center, University of Central Florida, 12424 Research Parkway Suite 400, Orlando, Florida 32816, United States
[d] College of Medicine, University of Central Florida, Orlando, Florida 32827, United states
[e] Corresponding authors email: Sudipta.Seal@ucf.edu, guptaankur@knights.ucf.edu

† Electronic Supplementary Information (ESI) available. See DOI: 10.1039/x0xx00000x

directly using electron spin resonance (ESR) spectroscopy; wherein, the reaction between titanium dioxide (TiO_2) and hydrogen peroxide (H_2O_2) was observed to generate ROS and inflammation [29]. Nano TiO_2 also induces cytotoxicity in peripheral blood lymphocytes, resulting in ROS and potential DNA damage [30]. Therefore, in cases of wear-debris evolution, the patient will need a revision surgery after a certain period of time. CNPs have demonstrated effectiveness in mitigating this inflammation in cells by scavenging ROS [31]. We hypothesize that a coating of cerium oxide on an implant surface can effectively scavenge ROS produced by the implant surface-cell interaction and have the potential to delay, possibly indefinitely, the need for revision surgery.

Detection of local ROS production is also challenging but advantageous for early therapeutic intervention. Though inorganic nanoparticles (e.g. CNPs and MoS_2) based electrochemical biosensors have shown ultra-low detection (pico-to nanomolar) of free radicals such as H_2O_2, HOCl and NO* [22,32], detachment of nanoparticles from implantable biosensors poses a substantial risk of toxicity and inflammation. The determined non-toxic nature of cerium oxide thin films and nanoparticles [20,33] can reduce/eliminate the concern of free-particle toxicity.

In the current work, nanoceria thin films with different thicknesses have been grown using an ALD technique and their surface chemistry has been analyzed in comparison to CNPs. Mimicking the surface chemistry of CNPs on ALD-grown cerium oxide coatings can be potentially used for many applications such as anti-inflammatory coatings, sensor platform, as a catalyst for chemical degradation, etc. To evaluate the potential efficacy of ALD ceria coating (ALD CeO_x) in biomedical applications, the biocatalytic activity has been tested and compared against cerium oxide nanoparticles (CNPs). Furthermore, to characterize film performance in a biosensor platform, ALD-grown CeO_x coatings have been used to sense H_2O_2, as a model system.

Experimental

Film deposition

Cerium precursor, tris(i-propylcyclopentadienyl)cerium [$Ce(iPrCp)_3$], was procured from Strem Chemicals, Inc., Newburyport, MA, USA. Analytical grade water (H_2O) was purchased from Sigma-Aldrich, USA. Water was used as an oxidizer during ALD process. Cerium oxide thin films were deposited in a Savannah S200 G2 ALD reactor (Ultratech/ Cambridge NanoTech, Waltham, MA, USA) equipped with low vapor pressure delivery (LVPD) kit. Cerium precursor $Ce(iPrCp)_3$ was contained in a stainless steel bubbler. The $Ce(iPrCp)_3$ was evaporated at 135 °C to generate enough vapor pressure for ALD. Bubbler valves and lines were maintained at 145 °C, whereas the manifold was kept at 160 °C. This temperature gradient was maintained during the deposition process to prevent the formation of a cold spot in precursor delivery line, thus the condensation of $Ce(iPrCp)_3$. H_2O cylinder was maintained at room temperature. Ultra-high purity (99.999%) nitrogen (N_2) was used as the carrier gas to carry the precursor vapors to the reactor chamber. N_2 was also utilized to purge the reactor between the precursor pulses. Cerium oxide thin films were deposited at 275 °C and temperature of the exhaust line was maintained at 150 °C. Deposition sequence consisted of two consecutive pulses of $Ce(iPrCp)_3$ (exposure time 2.5 sec), a 10 sec purge with N_2 followed by 0.05 sec exposure pulse of H_2O and a final 10 sec purge with N_2. Carrier gas flow was controlled at 80 sccm by a mass flow controller (MFC). Cerium oxide thin films were grown on silicon(100) substrates. Films of different thickness were deposited by changing ALD deposition cycles (50, 200, 500 and 1000). Schematic of the deposition process is shown in Fig. 1.

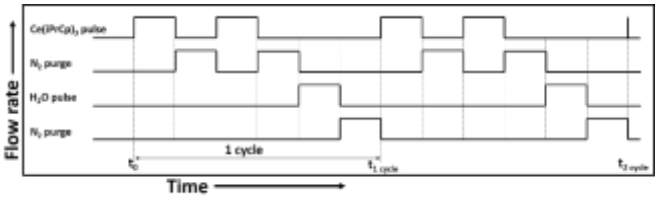

Figure 1: Precursor pulse and purge sequence used for the atomic layer deposition of cerium oxide (CeO_x) films. Two consecutive pulses of 2.5 s each of cerium precursor [$Ce(iPrCp)_3$] followed by 0.05 s pulse of H_2O was utilized for CeO_x films deposition. Low vapor pressure delivery kit (LVPD) was used for cerium precursor delivery due to its very low vapor pressure at room temperature and elevated temperature (135 °C). Si(100) was the used as substrate.

Film characterization

Ex-situ measurements were performed to determine the film thickness, structure, surface chemistry, and morphology. Film thickness was determined by X-ray reflectivity (XRR). A PANalytical X'Pert³ Materials Research Diffractometer (MRD) equipped with Cu-Kα radiation source was employed for XRR. The crystallinity of films was studied using Panalytical Empyrean having Cu-Kα radiation source. X-ray photoelectron spectrometer (XPS) measurements were performed on Thermo Scientific ESCALAB 250Xi spectrometer at room temperature in ultra-high vacuum (UHV) chamber (4×10^{-9} Torr) using Al-K_α radiation (binding energy 1486 eV). The spot size of the beam was approx. 250 µm. C 1s peak at 284.6 eV was used as a reference for calibration. The XPSPEAK41® software was utilized for deconvolution to identify the oxidation states of Ce (3d), O (1s), and Si (2p). The XPS fitting procedure is included in the electronic supplementary information. Grain size, coherency and orientation relation of ALD CeOx films were evaluated by high resolution transmission electron microscopy (HRTEM) using FEI Tecnai F30 operating at 300 keV. FEI 200 TEM FIB system was utilized to prepare ultra-thin (~100nm) sample for HRTEM. FTIR spectra were collected to identify the presence of residue left by metalorganic Ce precursor using PerkinElmer Spectrum One® spectrometers.

Bio-catalytic activity (H_2O_2 scavenging)

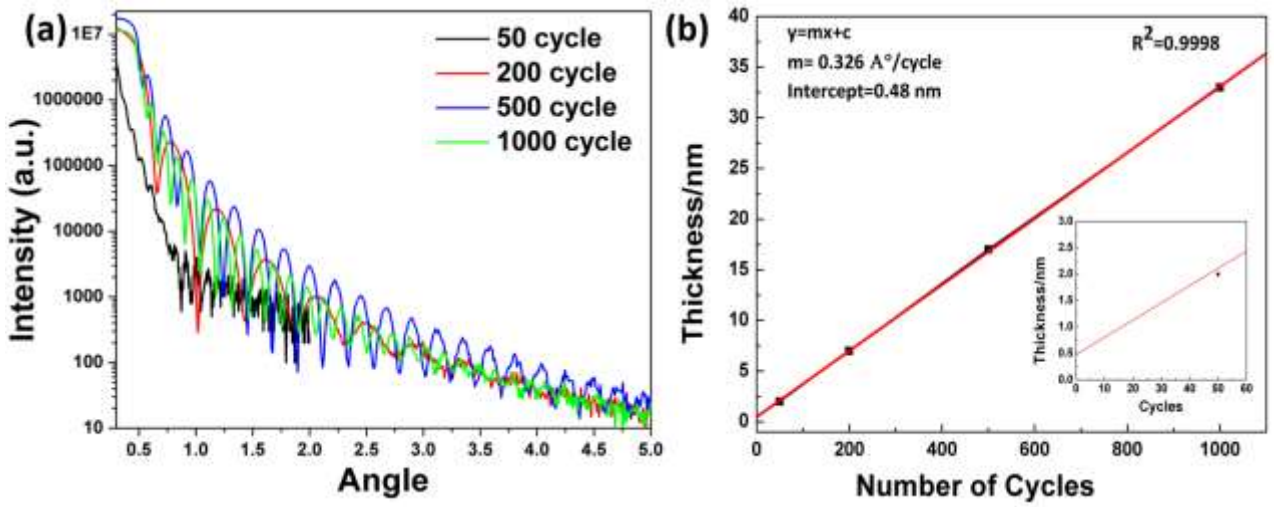

Figure 2: Estimation of film thickness and density. a) X-ray reflectivity (XRR) data of ALD CeO_x films of varying thickness. Well defined and sharp peaks indicate intermediate to high density and low surface roughness (< 1 nm) in the deposited coating. b) Thickness of CeO_x films as a function of the number of deposition cycles on a Si(100) at 275 °C. The linear relationship between film thickness and cycle number illustrates the self-limiting character of ALD. A growth rate of 0.33 Å/cycle was measured. The coefficient of linear fit (R^2) was 0.9998, strongly suggesting the described linear relationship.

Quantitative determination of catalase (CAT) mimetic activity of 50, 200, 500 and 1000 cycle CeOx samples was carried out using commercially available Amplexs Red® hydrogen peroxide assay kit [Invitrogen, Catalogue #A22188]. A minor modification wasd one from the standard protocol where the reaction was performed in 1 ml quartz cuvette with a total reaction mixture of 1 ml each. H_2O_2 concentration in the reaction mixture was kept at 1 µM and added in last to initiate the reaction. Control [H2O and Si(100)] and ALD CeOx samples were used for the reaction, and measurements were performed at 560 nm for a time duration of 20 minutes using the Perkin-Elmer Lambda 750S UV/Visible spectrometer and the data was plotted accordingly.

Cell culture

Mammalian cell toxicity assessment. Cell toxicity of the scratched particles from the coated film, was conducted on primary human skin keratinocyte (HaCaT) cell line (obtained from American Type Culture Collection (ATCC® PCS-200-011™)) for the preliminary results. In brief, HaCaT cells, maintained in DMEM:F12 media were trypsinized and were seeded in 96 well plate in the range of 10,000 cells/well in complete media. After overnight incubation, these cells were treated with different scratched particles at two different concentration (10 µM and 100 µM) for a time period of 48 hrs. Cell viability assay was performed using the Thiazolyl blue tetrazolium bromide (MTT, 0.5 mg/ml) after the incubation. Cells were washed with phosphate buffer saline (PBS) and 100 µl MTT (0.5mg/ml) was added to the respective well and subjected to 3 hrs of incubation. Cells were again washed with PBS and 100 µl of dimethyl sulfoxide (DMSO) were added. The ratio of the absorbance value of treated samples to untreated controls leads to cell viability analysis and the obtained data was presented in percentage with respect to controls.

Intercellular ROS estimation. Estimation of intracellular reactive oxygen species (ROS) scavenging property was also performed using the scratched particles from the coated film. In brief, HaCaT cells were seeded in the range of 10,000 cells per well in a 96 well fluorescent compatible plate and incubated overnight. Cells were washed with PBS and incubated with a known amount of H_2O_2 (100 µM) with the scratched particles at a concentration of 10 µM and further incubated for 24 hrs. After incubation, cells were washed with PBS and exposed to freshly prepared 50 mM DCFDA in PBS solution and incubated for 30 minutes. Further, these micro-plates were subjected to fluorescence spectrophotometry at 485 nm and data was analyzed. The amount of fluorescence intensity obtained is directly proportional to the amount of ROS present in the cells.

Biosensor for H_2O_2 detection

For electrochemical detection of the biologically relevant chemical hydrogen peroxide (H_2O_2), ALD film was grown on thin film glassy carbon electrodes (TFGCE) prepared through the carbonization of poly(acrylonitrile) (PAN) polymer [32]. A CeO_x film was deposited for 200 cycles using parameters discussed in film deposition section. TFGCE acts as a transducing layer. A three-electrode system i.e. Pt mesh as counter electrode, Ag/AgCl as reference electrode and TFGCE/CeO_x ALD as working electrode, was used for electrochemistry experiments. Bio-Logic SA VSP (Princeton Applied Research) system was used for all electrochemical experiments. All experiments were performed at room temperature and potentials were measured versus Ag/AgCl reference electrode. N_2-saturated 10 mM phosphate buffered saline (PBS) solution was utilized as an electrolyte during electrochemical experiments to minimize the interference from dissolved oxygen (O_2) gas. The same solution was used to dilute the 30 v/v% (9.8 M) H_2O_2 solution (Sigma-Aldrich, USA) to the desired concentration. Cyclic voltammetry (CV) was performed at 50 mV/s and in the range of (-0.3) to (0.7) V. This range was specifically chosen to prevent signals from

hydrolysis (oxidation at ~ -0.32 V and reduction at ~0.8 V). Chronoamperometry (CA) experiments were carried out at (-0.3) V to evaluate the sensitivity of H_2O_2 biosensor. The Pt mesh electrode was cleaned electrochemically per a procedure reported in published literature [32].

Results and discussions

The raw XRR data for ALD CeO_x films is presented in Fig. 2a. A Si(100) substrate, treated under similar condition (heated to 275°C, hold for 5 min followed by 10 pulses of 0.05sec of H_2O at an interval of 10 sec) in the ALD reactor, was used as a reference. The obtained data was fitted to a simulated curve using film thickness, density and surface roughness as fitting parameters. The thickness of ALD grown CeO_x films is plotted as a function of number of ALD deposition cycles, in Fig. 2b. Film thickness increases with increasing number of ALD cycles. Thicknesses of 2, 7, 17 and 33 nm correspond to 50, 200, 500 and 1000 cycles, respectively. Film density and surface roughness values were determined through regression ($R^2 \geq 0.98$) and were calculated as 5.55-6.13 g/cc (77-85%) and 0.52-0.67nm, respectively. The linear dependence is illustrative of the complete self-limiting growth reaction of CeO_x films and is characteristic of the ALD process. Self–limiting behavior of films reveal that two consecutive pulses of $Ce(iPrCp)_3$, each occurring over of 2.5 sec, followed by one 50 msec pulse of oxidizer (H_2O), is sufficient to produce CeO_x thin films utilizing a low vapor pressure delivery kit (LVPD) (Details of the optimization study of required Ce precursor pulses are provided in the supplementary information. It was reported that six pulses of $Ce(iPrCp)_3$ per cycle (H_2O as the oxidizer) at 250 °C is required to achieve the complete coverage of the substrate [34]. Our findings clearly demonstrate the importance of the LVPD kit for the deposition of thin films from very low vapor pressure precursors. The growth rate of the films, calculated as the linear regression functions slope, is 0.33 Å/cycle. Extrapolation of fitted data shows an intercept of 0.48 nm on the y-axis. This could arise from adsorbed water/Si-OH on the substrate surface.

The calculated growth rate (0.33 Å/cycle) is close to the reported values in literature [14,35]. Päivsaari *et al.* [35] obtained a growth rate of 0.32 Å/cycle and 0.34 Å/cycle for $Ce(thd)_4$ and $Ce(thd)_3$phne precursors with ozone, respectively. A growth rate of 0.35 Å/cycle has been reported for plasma enhanced (PE)-ALD process, where oxygen plasma was used to oxidize the Ce precursor and deposition was carried out at room temperature [14]. Comparison of previous studies to our findings shows that the use of oxygen plasma in ALD process can significantly bring down the CeO_2 deposition temperature without compromising growth rate. Another advantage associated with PE-ALD is the lower time required per cycle. Modification of the current Savannah S200 G2 ALD system to accommodate and installation of a plasma generator can significantly reduce the processing time for CeOx films of desired thickness. In this approach, plasma is generated in the active reaction zone for desired timestep/interval. Application of plasma in the current ALD process has two-fold benefits. (i) Radicals of Ce precursor will generate under plasma environment which are short lived but more reactive. Plasma removes the passivating functional group and activates the surface for the next monolayer of precursor. (ii) Use of plasma can bring down the deposition temperature. In the current process, CeOx films were deposited at 275°C. As a plasma source removes the passivating functional groups (from the precursor), thermal activation is not required. Therefore, films can be deposited at lower temperature. However, PE-ALD cannot compensate the substantial heating requirement of low vapor pressure precursors.

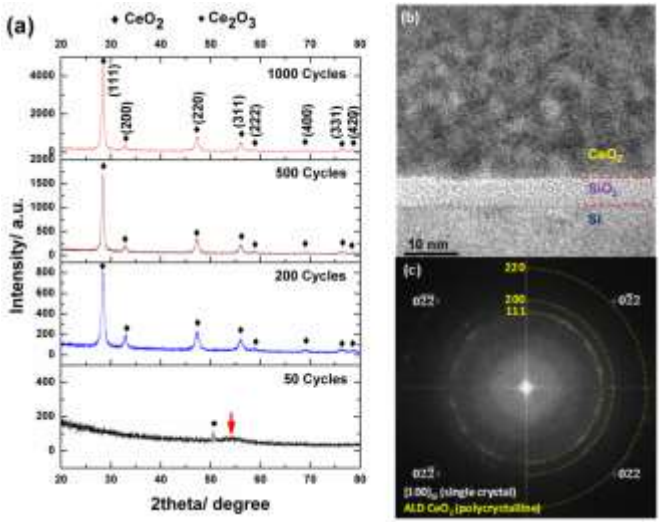

Figure 3: Structural characterization of ALD-grown CeO_x films. a) XRD spectrum of CeO_x films deposited for different ALD cycles on a Si (100) at 275 °C. Films deposited for cycles ≥200 cycles are of polycrystalline nature and consisted of CeO_2 phase. Lattice strain in the films decreases with increasing thickness (increasing ALD process deposition cycle). b) Bright-field TEM micrograph of 1000 cycle ALD CeO_x film shows distinct regions in the deposited films and their corresponding thickness. Random orientation of grain in the CeOx film suggest polycrystalline nature, supporting XRD data. c) Selected area electron diffraction (SAED) pattern taken from (b). Discrete spots (yellow broken line) confirm the polycrystalline nature of ALD-grown CeO_x films.

The crystallinity of deposited ALD CeO_x films was evaluated by XRD and is presented in Fig. 3a. Films deposited for 200, 500 and 1000 cycles are polycrystalline and clearly exhibit the (111), (200), (220) and (311) peaks of CeO_2. No preferred orientation was observed for films with a larger number of deposition cycles. However, literature reports post-deposition annealing treatment resulted in preferred (200) orientation [35,36]. The film deposited for only 50 cycles appears to be amorphous in nature. For 50 cycle sample, no sharp diffraction peaks are visible, except a minor peak at 50.62° (Fig. 3a, S1) which corresponds to Ce_2O_3 with trigonal crystal structure (space group $P\bar{3}m1$). A small amorphous peak close to CeO_2 (311) position was also observed (marked with red arrow) in the 50-cycle sample (Fig. 3a). This amorphous peak originates from the interaction of deposited CeOx with the SiOx/Si substrate which result in an amorphous extremely thin (~0.5-2 nm), and complex cerium-silicate interfacial phase (discussed in detail in the XPS section later). Thus, it can be anticipated that transformation from Ce_2O_3 in the 50 cycle sample, to CeO2 in the 200-1000 cycle samples occurs to relieve strain in

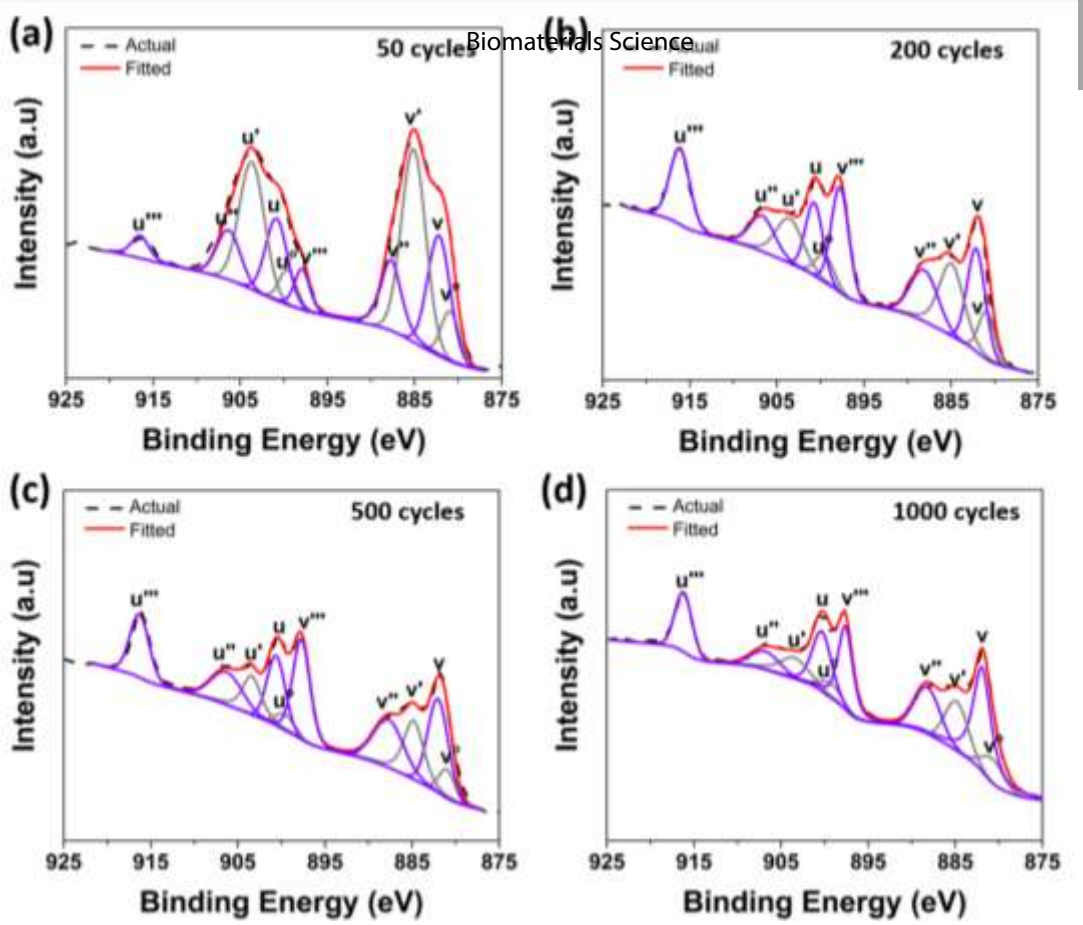

Figure 4: Surface oxidation state of ALD-grown CeO_x films. Deconvoluted and fitted XPS spectrum of Ce (3d) taken from different thickness CeO_x films a) 50 cycles, b) 200 cycles, c) 500 cycles and d) 1000 cycles. Decreasing intensity of peaks corresponding to Ce^{3+} (grey color) clearly indicate a decrease in Ce^{3+} concentration with increasing ALD process cycles. Highest [Ce^{3+}] measured in 50 cycle sample (54%) attributed to Ce-Si interaction at the interface and Ce_2O_3 formation. Further, Ce^{3+} oxidation state decreased from 34% (200 cycles) to 25% (1000 cycles). Tensile lattice strain and thermodynamic stability of cerium oxide result in decreasing Ce3+ concentration with increasing film thickness.

the films. It is known [37] that Ce_2O_3 phase is unstable due to the lattice strain in the material; it eventually converts into a CeO_2 phase, which is more thermodynamically stable. Thus, it can be envisioned that a 2-3 nm thin film has higher residual strain than 7-33 nm thick films. Strain in the films was calculated using the (220) diffraction peak to minimize error. The measured residual strains in the films were 1.23% (200 cycle), 0.91% (500 cycle) and 0.74% (1000 cycle). Absence of diffraction peaks in the 50 cycle sample restricted the strain calculation to high cycle samples only. The nature of residual strain in the ALD CeO_x films is tensile which arises due to the higher ionic radius of Ce^{3+} ions. The ionic radius of Ce^{3+} and Ce^{4+} ions are 1.034Å and 0.92Å, respectively [17]. The change in the ionic radius results in lattice distortion and tensile strain. Therefore, as the film thickness increases, residual strain decreases due to the relative greater presence of equilibrium phase (CeO_2).

To measure the grain size and orientation with respect to Si(100), TEM study was performed on 1000 cycle ALD CeO_x film. Figure 3b shows the interface region of the deposited film. Three distinct layers are observed i.e. (i) Si(100) substrate (Fig. S2e), (ii) amorphous SiO_2 (Fig. S2b) and (iii) ALD CeO_x (Fig. S2a). The thickness of the amorphous SiO_2 layer is ~5nm. It is clearly visible from Fig. 3b that no particular orientation relationship exists at the amorphous SiO_2 and ALD CeO_x interface. The interface appears very clean, suggesting low surface roughness of grown films. Furthermore, deposited films look highly dense. Therefore, both density and roughness, are in good agreement with XRR results. Randomly oriented lattice fringes in ALD CeO_x region indicates the polycrystalline nature of deposited films. Presence of discrete spots on concentric rings in the diffraction pattern (Fig. 3c) corresponds to CeO_2 lattice spacings, further confirming the polycrystalline structure of the film. This observation agrees well with the XRD spectrum. The grain size of the film ranges from 5 to 8 nm as measured from inverse FFT micrographs from HRTEM images of the film (see supporting information Fig. S3).

Extensive XPS studies were performed to further understand the growth mechanism and effect of growth cycles on the oxidation state of ALD CeO_x films. XPS surveys of deposited ALD CeO_x films are shown in Fig. S4. The identified peaks correspond to various x-ray photoelectron and Auger electron emissions in Ce, O, C and Si. A minor impurity peak of F1s (C-F_2) was also observed in the 50 cycle sample. F1s (C-F2) is a common impurity in reactors sealed with fluoroelastomer (Viton®) seals. De-convoluted XPS Ce (3d) spectrum of 50, 200, 500 and 1000 cycle deposited CeOx films are shown in Fig. 4. Peaks in the Ce (3d) spectrum can be distinguished and ascribed to unique oxidation states. Peaks v''', v'', v, u''', u'' and u belong to Ce^{4+}, and peaks v^0, v', u^0 and u' belong to Ce^{3+} [18]. For quantitative analysis of Ce ion oxidation states in different films,

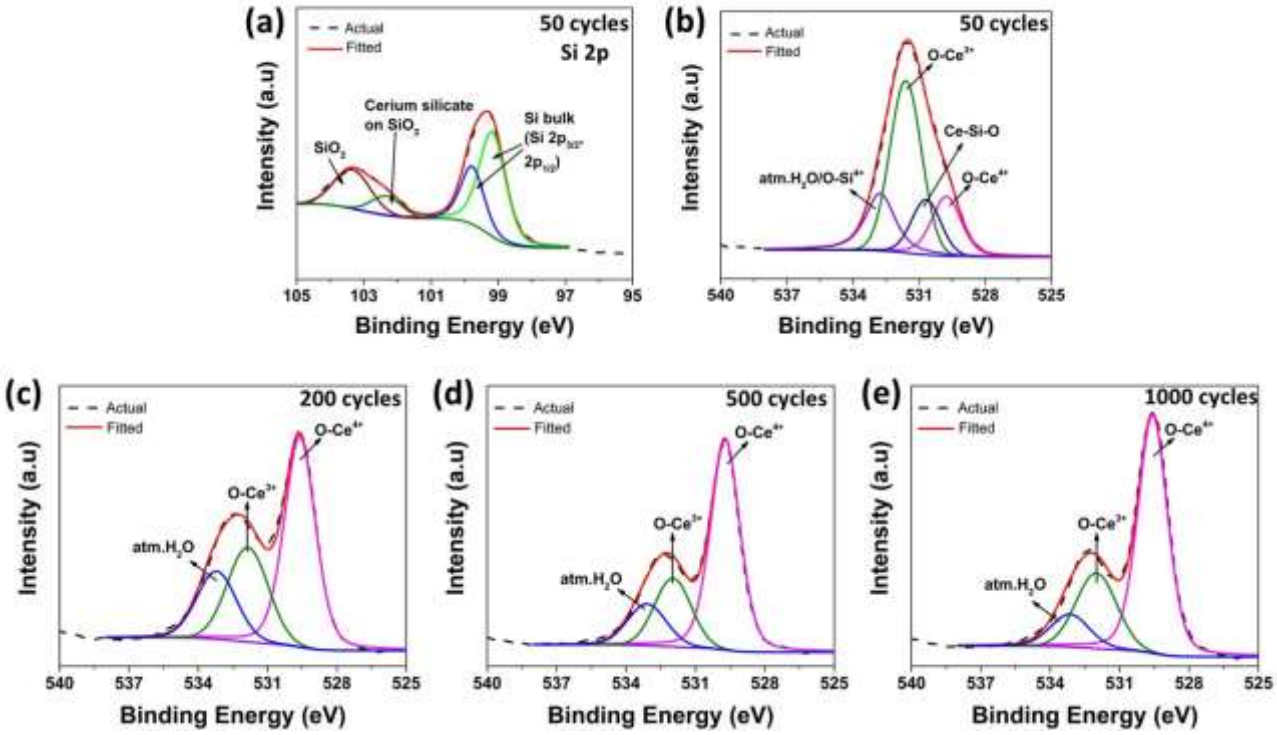

Figure 5: a) Deconvoluted XPS spectrum of Si (2p) collected from 50 cycle CeOx film. Deconvoluted and fitted XPS spectrum of O (1s) taken from different thickness CeOx films b) 50 cycles, c) 200 cycles, d) 500 cycles and e) 1000 cycles. The intensity of peaks corresponding to O-Ce3+ decrease with the number of increasing ALD process cycles. The intensity ratio (>1) of O-Ce3+ and O-Ce4+ for 50 cycles sample further provide the evidence of suitable micro-environment in the lattice to accommodate high concentration (54%) of Ce3+ ions. This is attributed to the formation of cerium silicate phase at the interface in 50 cycle sample. Ce exists in Ce3+ oxidation state by reducing the SiO2 to form cerium silicate phase. This is confirmed by the presence of Ce-Si-O peak in both O (1s) and Si (2p) spectra.

various peaks present in the XPS spectrum, which appear due to the $3d_{5/2}$ and $3d_{3/2}$ spin-orbital splitting, were fitted with a Gaussian-Lorentzian distribution. The ratio of the total area under the fitted peak of Ce^{3+} to the total area of all peaks (Ce^{3+} and Ce^{4+}) gives the concentration of Ce^{3+} in films (Equation 1, where A_i is the integrated area of peak i). The relative concentration of Ce^{3+} and Ce^{4+} ions on the surface of CeO_x films are presented in Table 1.

$$[Ce^{3+}] = \frac{A_{v0}+A_{v'}+A_{u0}+A_{u'}}{A_{v0}+A_{v'}+A_{u0}+A_{u'}+A_{v'''}+A_{v''}+A_{v}+A_{u'''}+A_{u''}+A_{u}} \qquad (1)$$

XPS analysis reflects that the highest concentration (54%) of surface Ce^{3+} ions is found for 2 nm CeO_x film. Surface Ce^{3+} ion concentration drops sharply from 54% to 34% for 7 nm CeO_x film and remains in the range of 25-26% for higher cycle samples (7 and 33 nm thickness samples). The decrease in surface Ce^{3+} concentration is also visible in the deconvoluted Ce (3d) XPS spectrum. The peak at 916 eV in the Ce (3d) XPS spectrum (Fig. 4) corresponds to Ce^{4+}. Thus, any change in the intensity of this peak, relative to other peaks, provides qualitative information with respect to the relative difference in concentration of each oxidation state. The intensity of the peak at 916 eV is significantly lower for 50 cycle CeO_x film compared to the rest of the higher thickness CeO_x films.

To maintain the charge balance, substitution of one Ce4+ ion from cerium oxide lattice by Ce3+ creates two oxygen vacancies in the lattice. Therefore, it can be stated that 2 nm thick CeOx films have significantly higher oxygen lattice vacancies because

Table 1 Summary of the surface oxidation state of Ce (3d) from XPS.

Sample	Ce^{3+} [%]	Ce^{4+} [%]
50 cycle	54	46
200 cycle	34	66
500 cycle	26	74
1000 cycle	25	75

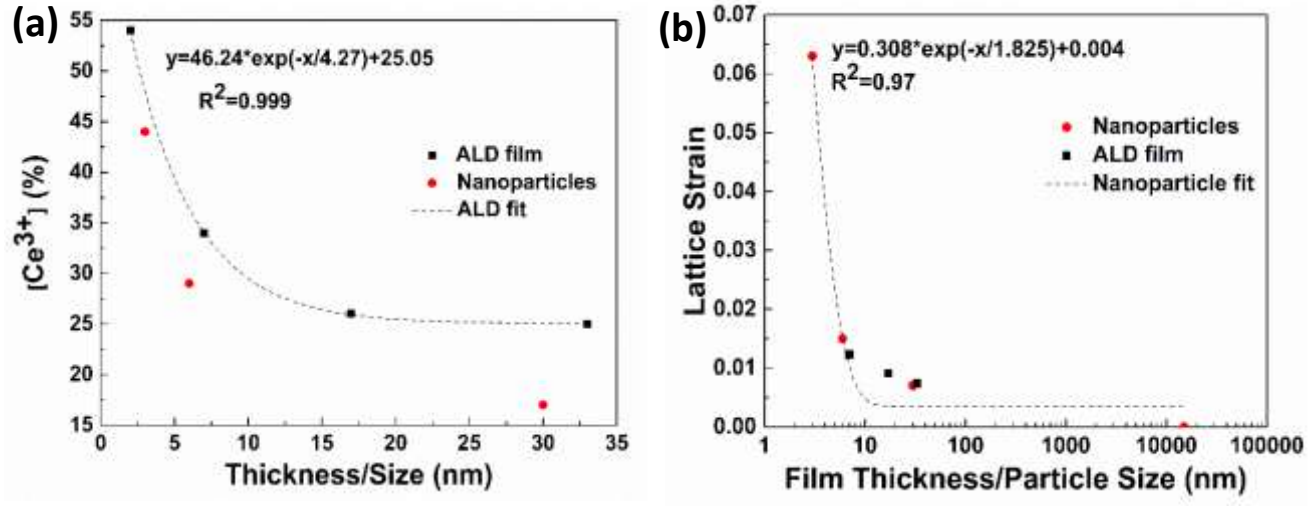

Figure 6: Comparison of ALD-grown CeO_x films with nanoceria particles (CNPs). a) Ce^{3+} concentration and b) lattice strain in ALD CeO_x films and CNPs as a function of thickness and particle size, respectively. Ce^{3+} ions concentration and lattice strain in both, ALD CeO_x films and CNPs show good correlation, thus indicating the common surface chemistry of CNPs and ALD-grown CeO_x films.

x-ray photoelectrons emit only from 4-5 nm depth of the samples. Since the thickness of the sample is only 2 nm, XPS can provide the exact chemical composition for the entire film volume, in the present case. This was verified by collecting the Si (2p) spectrum presented in Fig. 5a and Fig. S5. Peaks of SiO_2, cerium silicate and bulk Si (2p) are existing only in 50 cycle sample because of its thickness (2 nm). No peaks of bulk Si (2p), cerium silicate and SiO_2 were observed in 200, 500 and 1000 cycle samples because the thickness of films is higher than the depth of photoelectron emission (see Fig. S5). The intensity of O-Ce^{3+} peak in O (1s) spectrum collected from 50 cycle sample is higher than O-Ce^{4+} peak (O-Ce^{3+}/O-Ce^{4+} > 1) (Fig. 5b). However, the O-Ce^{4+} peak is more intense than the O-Ce^{3+} peak in case of 200, 500 and 1000 cycle samples (O-Ce^{3+}/O-Ce^{4+} < 1) (Fig. 5c-d). An additional peak at 530.6 eV is identified in the deconvoluted O (1s) spectra of 50 cycle sample (Fig. 5b) which is absent in the higher cycle samples. According to the literature, CeO_2 thin films deposited on SiO_2/Si substrates using e-beam evaporation [38], reactive evaporation [39], rf magnetron sputtering [40] etc.,form an amorphous cerium-silicate phase at the interface. Therefore, a minor amorphous peak observed in the XRD spectrum of 50 cycle sample (Fig. 3a) can be assigned to the cerium silicate interlayer. Vorokhta et al. [40] have suggested that Ce reduces the silicon oxide to form cerium silicate where it bound in Ce^{3+} oxidation state. Various thickness of cerium silicate interlayer from 0.3-1.1 nm is reported in the literature [38-40]. These reported thicknesses are lower than the thickness of 50 cycle sample prepared in the current study. Presence of a strong O-Ce^{3+} peak in the O (1s) spectra and a small peak corresponding to Ce_2O_3 phase in the XRD (Fig. 3a) indicate that cerium silicate layer is sandwiched between Si(100) substrate and Ce_2O_3 layer. Formation of cerium silicate is further confirmed by the presence of an additional peak in Si (2p) spectra in Si (2p) spectra of 50 cycle sample at 102.3 eV (Fig. 5a). Therefore, higher Ce^{3+} concentration in 50 cycle sample is arising from both, cerium silicate and Ce_2O_3. O1s spectra analysis further support our findings from deconvoluted Ce (3d) spectrum that Ce^{3+} concentration is higher in 50 cycle film compared to the higher thickness films and consists of ~50% oxygen vacancies. This finding is in good agreement with the calculated surface Ce^{3+} concentration.

The presence of –OH (atm.H_2O), O-Ce^{3+}, O-Ce^{4+} and Ce-Si-O peaks also provide valuable insight into CeO_x film formation and its transformation from Ce^{3+}-rich surface to Ce^{4+}-rich surface. During the ALD process, Ce precursor reacts with the hydroxyl groups present on the substrate, liberating i-propylcyclopentadienyl molecule. The reaction is self-limiting as the Ce precursor does not react with adsorbed Ce species. Unreacted precursor and liberated i-propylcyclopentadienyl was removed from the reactor by carrier gas (N_2). In the next step, H2O reacts with i-propylcyclopentadienyl groups on deposited Ce atoms forming both Ce-O-Ce bridges and new hydroxyl groups (-OH) which prepare the surface for the next layer deposition. Thus, both Ce-O-Ce and -Ce-OH form on the surface. The deposited Ce reacts with the native amorphous SiO_2 layer, thus forming an amorphous cerium silicate interlayer of thickness < 2nm. CeOx layer continue to grow over the cerium silicate interlayer with increasing number of ALD cycles. Decrease in Ce^{3+} surface concentration and residual strain with increasing film thickness further supports our proposed growth mechanism. Additionally, in the case of CeO_2 nanoparticle preparation using wet chemical process, cerium hydroxide ($Ce(OH)_3$) forms first, which further converts into CeO_2 to attain the equilibrium energy state [41]: identical to our proposed growth mechanism. The intensity of the –OH peak decreases with increasing deposition cycles; indicating that in the ALD CeO_x deposition, $Ce(iPrCp)_3$ precursor reacts with H_2O and forms $Ce(OH)_3$. The cerium hydroxide intermediate further converts Ce_2O_3 to CeO_2 with increasing ALD cycles. Also, amorphous to crystalline transformation occurs in films as indicated by XRD analysis and is additional evidence of film growth. Furthermore, the presence of very high intensity –OH peaks, observed in deconvoluted O (1s) spectrum of 50 cycle samples, indicate the formation of $Ce(OH)_3$ in the ALD growth process (Fig. 5b). presence of –OH

peak also arises because the ALD deposition process was terminated with a H_2O pulse, leaving -OH groups on the surface. However, the relative intensity of O-Ce^{3+} peaks clearly indicate the dominance of $Ce(OH)_3$ than surface -OH groups in 50 cycle sample. The intensity of -OH peak is relatively lower for 200, 500 and 1000 cycle samples (Fig. 5) as more cerium oxide exist in equilibrium CeO_2 phase. The comparison of lattice strain and concentration of Ce^{3+} oxidation state present on the surface of ALD CeO_x films grown in the present study, and data collected from previous reports [18] on nanoceria (CNPs) of different size (3, 6 and 30 nm), is presented in Fig. 6. It is evident from Fig. 6a that the surface chemistry of ALD CeO_x films follow the CNPs trend. Thus, the surface chemistry of CNPs can be mimicked via ALD of CeO_x films with the thickness of films is limited to less than 10 nm. The common relationship between size and Ce^{3+}/Ce^{4+} for nanoceria is further corroborated by the comparative lattice strain in ALD CeO_x films (Fig. 6b). It can be observed that there

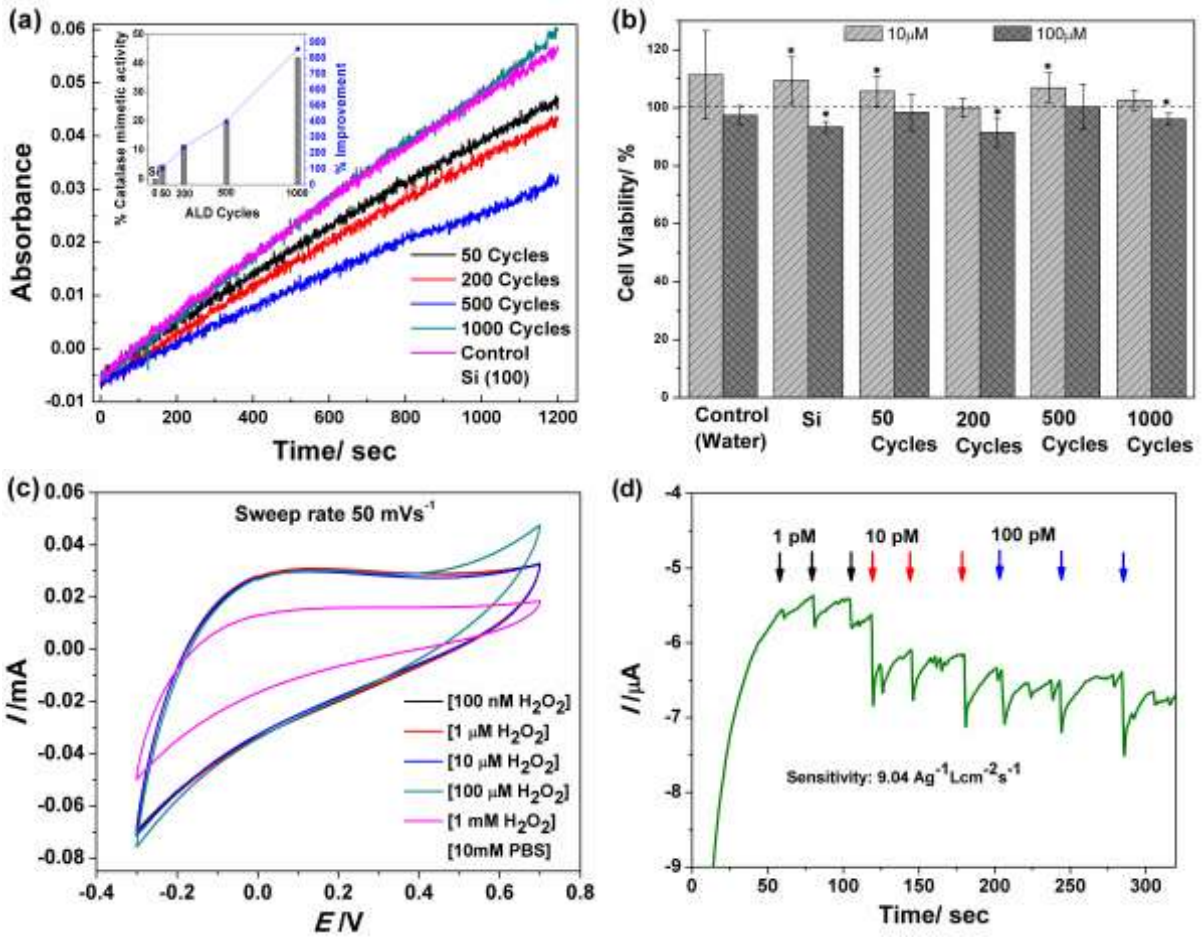

Figure 7: Bio-catalytic activity, in-vitro cell culture and electrochemical characterization. a) Thickness-dependent catalase-mimetic activity of ALD CeO_x films deposited for different number of cycles. Catalase-mimetic activity of ALD-grown CeO_x films increasing with film thickness. The 1000 cycles sample has 9-fold catalase-mimetic activity in comparison to the 50 cycles sample. b) Cell viability of HaCaT at two different concentrations (10 and 100 μ_M) for different cycle CeOx films. No abnormality in cell growth/death indicates the suppression of inflammatory reaction due to the redox character of CeOx simulated wear debris. The mean of 3 independent cultures is plotted with standard deviation; *, $p \leq 0.05$. c) Cyclic voltammograms response of 200 cycles deposited ALD CeO_x electrode in 10 mM PBS electrolyte at 50 mVs^{-1} scan rate with varying [H_2O_2]. d) The chronoamperometric response of 200 cycles deposited ALD CeO_x electrode towards H_2O_2 in 10 m_M PBS electrolyte. The measured limit of quantification is 1 p_M well below the physiological concentration in human body.

is a monotonous decrease in the lattice strain with increasing particle size and film thickness. Since the initial discovery of nanoscale cerium oxide's unique redox-active property, catalase-mimetic assay has become the experimental standard in evaluating ROS scavenging ability as a function of surface chemistry [42,43]. Therefore, the bio-catalytic property of ALD-grown CeO_x films was also evaluated in the form of catalase-mimetic activity to compare against our earlier findings. It is evident from Fig. 7a that the 1000 cycle sample has the highest catalase mimetic activity (42%, see inset of Fig. 7a) and it decreases linearly with decreasing number of deposition cycles. In other words, the catalase-mimetic activity of CeO_x films decreases with increasing surface Ce^{3+} concentration. The 50 cycle sample only has 4.9% catalase-mimetic activity. Therefore, the 1000 cycle sample is 9 times more catalase active then the 50 cycle sample (see inset of Fig. 7a). The 1000 cycle sample only has 25% surface Ce^{3+} concentration, whereas 50 cycle sample has 54% Ce^{3+} at the film surface. We have previously reported that the biocatalytic properties of CNPs prepared by different methods depends on the Ce^{3+}/Ce^{4+} ratio [17,19]. Higher Ce^{3+}/Ce^{4+} CNPs have SOD-mimetic and OH* scavenging activity, whereas lower Ce^{3+}/Ce^{4+} CNPs have catalase (H_2O_2) mimetic and NO* scavenging activity. Therefore, the catalase mimetic activity of ALD CeO_x films results appear to be in good correlation with our previously published reports. Additionally, catalase assay results confirm that the trends in particle size/lattice strain and Ce^{3+}/Ce^{4+} observed for ceria nanoparticles are paralleled by thin films produced through ALD at 275 °C.

One of the intended applications of developed ALD CeO_x films is to mitigate the inflammation response in patients who have undergone implant surgery in the event of osteolysis/wear debris generated due to physical motion. Further, in-vitro cell viability study was conducted on wear debris obtained from scratching. This study is essential to understand the behaviour of wear debris and effect of CeO_x coatings on wear debris towards uncontrolled tissue/cell growth around the implant. To assess the effect of surface chemistry and wear debris in a biological model, HaCaT cells were cultured and exposed to two different concentrations (10 and 100 μM) of scratched wear debris coated with CeO_x. The purpose of our study is to evaluate the anti-inflammatory activity, characterized as inter-cellular ROS scavenging, of ALD-deposited CeOx thin films. A HaCaT cell line culture was used to test for material general toxicity; due to the sensitivity of this line towards inflammation and its resulting predominance in toxicity literature. Results of an in-vitro cell viability study are presented in Fig. 7b. Results of the cell viability study show no adverse toxicity ($P<0.05$) toward HaCaT cells in the presence of ALD CeO_x-coated wear debris for the concentrations range 10–100 μM. Efficacy of ALD CeO_x films towards ROS scavenging was also analyzed, in vitro, by incubating HaCaT cells with 100 μM H_2O_2 and 10 μM wear debris. Subsequently, the remaining ROS, in the form of H_2O_2, was measured using fluorescence spectroscopy (Fig. S7). Fluorescence data showed that all ALD CeO_x films were able to scavenge significant amounts of intracellular ROS, as a function of surface chemistry. The fluorescence intensity decreases with increasing ALD cycle samples. The fluorescence intensity of the 1000 cycle sample and control (water) sample has an overlap demonstrating complete scavenging of ROS (H_2O_2) from the culture media. Results of quantification intercellular ROS scavenging activity are in good correlation with catalase-mimetic activity (Fig. 7a). It is evident from Fig. 7a,b and S7 that ALD CeO_x films show great promise in the potentiation of implant surgery-mediated inflammation.

To further extend the application of ALD CeO_x films, ALD-prepared CeO_x electrodes were also characterized in presence of H_2O_2. The relevance of this interaction comes from the prevalence of H_2O_2 as a product of free radicals in the body, which accumulate in instances of pathology (i.e. concentration correlates with progression of disease states such as cancers, diabetes, neurodegenerative diseases). Cyclic voltammetry (CV) was performed to characterize the electrochemical behavior of ALD CeO_x in presence of H_2O_2. Voltammetry was performed in the range of (-0.3) to (0.7) V at 50 mV/s. This range was specifically chosen to prevent signals from hydrolysis (oxidation at ~ -0.32 V and reduction at ~0.8 V) [22,32]. Measurements show (Fig. 7c) an increase in reduction current at -0.3 V in presence of H_2O_2 and a positive correlation between concentration and current at this potential. This observation is supported by other findings in related works [22,44] and represents the reduction of peroxy groups at the surface of CeO_x. To be certain that the observed peak is characteristic of H_2O_2 reduction at surface sites and not from elaborate surface reactions or Galvanic responses: CV was performed at varying scan rates. The trend in current increase with increasing scan rate suggests that the response is diffusion limited (Fig. S8). Inputting these values in the Randles-Sevcik equation confirms this behavior. However, the absence of an obvious corresponding oxidation peak suggests that this reaction is irreversible. This determination is reasonable given the radical nature of the H_2O_2 analyte (i.e. relatively low stability, high reactivity). In order to use ALD CeO_x electrodes as biosensors, the described electrochemical reaction must produce a consistent signal response in presence of specific concentrations of analyte. However, CV can be less consistent/reliable and is not appropriate for these analyses. Therefore, chronoamperometry (CA) was utilized at (-0.3) V, per the observed electrochemical response in CV.

Chronoamperometry (CA) was performed by applying a constant potential and spiking the test solution with known concentrations of H_2O_2 under N_2 gas purging to mix the test solution. Current response was immediate (time of response ~8 s; time from addition of analyte to equilibration of current signal baseline), following the addition of analyte. Additionally, current response was reliable (mean response for 10nM: 0.420 μA, SD: 0.0464 μA) (Fig. 7d). The addition of different concentrations of H_2O_2 shows increasing current with increasing analyte concentration. The sensitivity of ALD CeO_x biosensor was determined to be 9.04 $A*L/g*cm^2*s$ based on the current response. Further, the limit of quantitation (LOQ) was determined to be ~1 pM using CA. This value was determined using the conventional description,

LOQ = (Root Mean Square of Blank current) + 10 σRMS, Blank (2)

Detection at this ultra-low concentration is highly significant, as disease states can be detected at very early stages as well as in low volume or dilute samples of bio-fluid. This sensor is several orders of magnitude below that of the reviewed sensors: both enzymatic and inorganic-based sensors [22,32]. Ceria has been shown elsewhere to be highly specific towards reactive oxygen species (ROS) [17,42,45,46]. In a recent study, we have shown that none of glucose, nitrite, nor uric acid interfering species elicit current signals from the ceria sensor [22]. These results speak to the high degree of selectivity posed by cerium oxide-based sensor. Use of an inorganic oxide thin film, CeO_x, as the detection element of the sensor allows for a highly robust device/detection. Ceria is largely insensitive to heating and will not lose activity, as enzymes do, when exposed to varied conditions demonstrated in our earlier publication [22]. Furthermore, detachment of nanoparticle-based implantable biosensor can pose a risk of potential toxicity. Non-toxic nature of cerium oxide nanoparticles (CNPs) [20,33,47] and ALD CeO_x (Fig. 7b) film based biosensors reduce/eliminate the concern of toxicity. In fact, superior catalase mimetic activity of CNPs and ALD CeO_x (Fig. 7a) scavenge ROS and mitigate their adverse effect (Fig. 7b).

Conclusions

Cerium oxide (CeO_x) thin films of various thicknesses were successfully deposited on Si (100) substrates via an atomic layer deposition (ALD) method. The self-limiting character of the ALD chemical process was observed as a linear relationship between thickness and deposition cycles; with a growth rate of 0.33 Å/cycle. XRD characterization indicated that a Ce_2O_3 phase nucleates initially and is subsequently converted into CeO_2 phase with an increasing number of deposition cycles. Formation of these phases, following a given number of cycles, was further confirmed via XPS analysis. Specifically, an increase in surface Ce^{3+} redox state (25% to 54%), relative to Ce^{4+}, was observed with decreasing film thickness. The high concentration of Ce^{3+} ions in low thickness films is attributed to the cerium silicate interlayer formation followed by Ce_2O_3 layer deposition. This study also demonstrated an increasing catalase-mimetic activity with increasing film thickness. Thicker films showed excellent catalase-mimetic activity (9-fold) in proportion with film thickness and inversely with Ce^{3+}/Ce^{4+} ratio. In assessing the ALD-grown cerium oxide films potential as biocompatible implant coatings and as active layers for biomedical devices, cell viability and electrochemical studies were conducted. CeO_x-coated silicon particles showed minimal (<4%) apoptosis for HaCaT keratinocyte cultures via MTT assay, in vitro. Additionally, CeO_x films formed over glassy carbon electrodes were sensitive to 1 pM hydrogen peroxide. Overall, the ALD-formed CeO_x films, detailed herein, show promise for use as biomedical implant coatings and for use in sensor devices with controllable activity (via Ce^{3+}/Ce^{4+} modulation).

Conflicts of interest

There are no conflicts to declare.

Acknowledgement

The authors would like to thank the Materials Characterization facility at UCF for allowing the authors to utilize the characterization facilities. S.S acknowledges NSF MRI XPS: ECCS:1726636 for XPS.

Supporting information

Additional characterization data are provided, including Broader view of XRD spectrum of CeOx films, Inverse Fast-Fourier Transformation (FFT) images constructed from HRTEM of CeOx films used for grain size measurement, XPS survey spectra, FTIR spectra, Quantification of intracellular ROS scavenging properties of CeOx films, and Cyclic voltammograms response of 200 cycle deposited ALD CeOx electrode in with varying scan rate. Supplementary data to this article can be found online.

References

1 I. Shitanda, S. Mori and M. Itagaki, *Anal. Sci.*, 2011, **27**, 1049.
2 N. Izu, W. Shin, I. Matsubara and N. Murayama, *Sens. Actuat. B*, 2004, **100**, 411.
3 N. Mahato, A. Banerjee, A. Gupta, S. Omar and K. Balani, *Prog. Mater. Sci.*, 2015, **72**, 141.
4 T. X. Sayle, M. Cantoni, U. M. Bhatta, S. C. Parker, S. R. Hall, G. Möbus, M. Molinari, D. Reid, S. Seal and D. C. Sayle, *Chem. Mater.*, 2012, **24**, 1811.
5 A. Karakoti, J. King, A. Vincent and S. Seal, *Appl. Catal. A*, 2010, **388**, 262.
6 R. Z. Zand, K. Verbeken and A. Adriaens, *Int. J. Electrochem. Sci.*, 2013, **8**, 4924.
7 T. Dudziak, L. Boron, A. Gupta, S. Saraf, P. Skierski, S. Seal, N. Sobczak and R. Purgert, *Corrosion Science*, 2018, **128**, 326.
8 Y. -H. Kim, S. -K. Kim, N. Kim, J. -G. Park and U. Paik, *Ultramicroscopy*, 2008, **108**, 1292.
9 H. Lei, F. Chu, B. Xiao, X. Tu, H. Xu and H. Qiu, *Microelectron. Eng.*, 2010, **87**, 1747.
10 C. Zhao, C. Z. Zhao, M. Werner, S. Taylor, P. Chalker and P. King, *Nanoscale Res. Lett.*, 2013, **8**, 172.
11 P. F. Wahid, K. B. Sundaram and P. J. Sisk, *Opt. Laser Technol.*, 1992, **24**, 263.
12 J. Qiao and C. Y. Yang, *Mater. Sci. Eng. R*, 1995, **14**, 157.
13 F. Wang and R. Wördenweber, *Thin Solid Films*, 1993, **227**, 200-204.
14 W. -H. Kim, M. -K. Kim, W. J. Maeng, J. Gatineau, V. Pallem, C. Dussarrat, A. Noori, D. Thompson, S. Chu and H. Kim, *J. Electrochem. Soc.*, 2011, **158**, G169.
15 C. -H. Chen, I. Y. -K. Chang, J. Y. -M. Lee and F. -C. Chiu, *Appl. Phys. Lett.*, 2008, **92**, 043507.
16 S. Guo, H. Arwin, S. N. Jacobsen, K. Järrendahl and U. Helmersson, *J. Appl. Phys.*, 1995, **77**, 5369.
17 A. Gupta, S. Das, C. J. Neal and S. Seal, *J. Mater. Chem. B*, 2016, **4**, 3195.
18 S. Deshpande, S. Patil, S. V. Kuchibhatla and S. Seal, *Appl. Phys. Lett.*, 2005, **87**, 133113.
19 S. Das, J. Dowding, K. Klump, J. McGinnis, W. Self and S. Seal, *Nanomedicine (London, U. K.)*, 2013, **8**, 1483.

20 S. S. Lee, W. Song, M. Cho, H. L. Puppala, P. Nguyen, H. Zhu, L. Segatori and V. L. Colvin, *ACS Nano*, 2013, **7**, 9693.
21 P. Chaturvedi, D. C. Vanegas, M. Taguchi, S. L. Burrs, P. Sharma and E. S. McLamore, *Biosens. Bioelectron.*, 2014, **58**, 179.
22 C. J. Neal, A. Gupta, S. Barkam, S. Saraf, S. Das, H. J. Cho and S. Seal, *Sci. Rep.*, 2017, **7**, 1324.
23 A. Kumar, R. Devanathan, V. Shutthanandan, S. V. N. T. Kuchibhatla, A. S. Karakoti, Y. Yong, S. Thevuthasan and S. Seal, *J. Phys. Chem. C*, 2012, **116**, 361.
24 M. Hijaz, S. Das, I. Mert, A. Gupta, Z. Al-Wahab, C. Tebbe, S. Dar, J. Chhina, S. Giri, A. Munkarah, S. Seal and R. Rattan, *BMC Cancer*, 2016, **16**, 220.
25 M. Sack, L. Alili, E. Karaman, S. Das, A. Gupta, S. Seal and P. Brenneisen, *Mol. Cancer Ther.*, 2014, **13**, 1740.
26 C. K. Kim, T. Kim, I. -Y. Choi, M. Soh, D. Kim, Y. -J. Kim, H. Jang, H. -S. Yang, J. Y. Kim, H. -K. Park, S. P. Park, S. Park, T. Yu, B. -W. Yoon, S. -H. Lee and T. Hyeon, *Angew. Chem. Int. Ed.*, 2012, **51**, 11039.
27 K. L. Heckman, W. DeCoteau, A. Estevez, K. J. Reed, W. Costanzo, D. Sanford, J. C. Leiter, J. Clauss, K. Knapp, C. Gomez, P. Mullen, E. Rathbun, K. Prime, J. Marini, J. Patchefsky, A. S. Patchefsky, R. K. Hailstone and J. S. Erlichman, *ACS Nano*, 2013, **7**, 10582.
28 L. Jinhua, W. Jin, L. Bin, L. Wan, Q. Wei, S. Jie, J. Weihong, J. Xinquan, Y. K. W. K. and C. P. K., *Adv. Sci.*, 2018, **5**, 1700678.
29 M. C. Lee, F. Yoshino, H. Shoji, S. Takahashi, K. Todoki, S. Shimada and K. Kuse-Barouch, *J. Dent. Res.*, 2005, **84**, 178.
30 S. J. Kang, B. M. Kim, Y. J. Lee and H. W. Chung, *Enviro. Mol. Mutagen.*, 2008, **49**, 399.
31 S. Del Turco, G. Ciofani, V. Cappello, T. Navarra, C. Caselli, M. Gemmi, V. Mattoli and G. Basta, *Eur. Heart J.*, 2013, **34**, P4174.
32 A. Gupta, T. B. Rawal, C. J. Neal, S. Das, T. S. Rahman and S. Seal, *2D Mater.*, 2017, **4**, 025077.
33 J. M. Dowding, S. Das, A. Kumar, T. Dosani, R. McCormack, A. Gupta, T. X. T. Sayle, D. C. Sayle, L. von Kalm, S. Seal and W. T. Self, *ACS Nano*, 2013, **7**, 4855.
34 R. R. Essex, J. I. Ressero, G. M. Jursich and C. G. Takoudis, *J. Undergrad. Res.*, 2013, **6**, 37.
35 J. Paivasaari, M. Putkonen and L. Niinisto, *J. Mater. Chem.*, 2002, **12**, 1828.
36 L. Kim, J. Kim, D. Jung, C. -Y. Park, C. -W. Yang and Y. Roh, *Thin Solid Films*, 2000, **360**, 154.
37 R. C. Merrifield, K. P. Arkill, R. E. Palmer and J. R. Lead, *Environ. Sci. Technol.*, 2017, **51**, 8010.
38 E. J. Preisler, O. J. Marsh, R. A. Beach and T. C. McGill, *Journal of Vacuum Science & Technology B: Microelectronics and Nanometer Structures Processing, Measurement, and Phenomena,* 2001, **19**, 1611.
39 F. Pagliuca, P. Luches and S. Valeri, *Surface Science*, 2013, **607**, 164.
40 M. Vorokhta, I. Matolínová, M. Dubau, S. Haviar, I. Khalakhan, K. Ševčíková, T. Mori, H. Yoshikawa and V. Matolín, *Applied Surface Science*, 2014, **303,** 46.
41 T. Sakthival, S. Das, A. Kumar, D. L. Reid, A. Gupta, D. C. Sayle and S. Seal, *ChemPlusChem*, 2013, **78**, 1446.
42 C. Korsvik, S. Patil, S. Seal and W. Self, *Chem. Commun.*, 2007, 1056.
43 E. G. Heckert, A. S. Karakoti, S. Seal and W. T. Self, *Biomaterials*, 2008, **29**, 2705.
44 N. P. Sardesai, D. Andreescu and S. Andreescu, *J. Am. Chem. Soc.*, 2013, **135**, 16770.
45 J. Dowding, T. Dosani, A. Kumar, S. Seal and W. Self, *Chem. Commun.*, 2012, **48**, 4896.
46 J. M. Dowding, S. Seal and W. T. Self, *Drug Deliv. Transl. Res.*, 2013, **3**, 375.
47 A. Gupta, S. Das and S. Seal, *Nanomedicine (London, England)*, 2014, **9**, 2725.

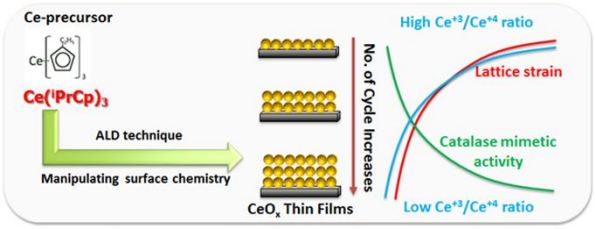

Precise control of ceria surface chemistry in ALD-grown thin films as a platform for biocompatible coating